CHEMISTRY OF MATERIALS

pubs.acs.org/cm

Article

In Situ High-Temperature Structural Analysis of High-Entropy Rare-Earth Sesquioxides

Matheus Pianassola,* Kaden Anderson, Can Agca, Chris J. Benmore, Jake W. McMurray, Jöerg C. Neuefeind, Charles Melcher, and Mariya Zhuravleva

Cite This: *Chem. Mater.* 2023, 35, 1116–1124

Read Online

ACCESS | Metrics & More | Article Recommendations | Supporting Information

ABSTRACT: High-entropy rare-earth (RE) sesquioxides (RE_2O_3) containing five cations in equimolar amounts have been investigated for a variety of applications, but little is known about their polymorphic behavior and coefficient of thermal expansion. Here, we evaluate the effect of the average ionic radius (AIR) on the polymorphism of high-entropy RE_2O_3. Powder samples of compositions 1 $(Lu,Y,Ho,Nd,La)_2O_3$ (AIR = 0.938 Å) and 2 $(Gd,Eu,Sm,Nd,La)_2O_3$ (AIR = 0.982 Å) were synthesized via a wet chemical method, and bead samples were prepared for aerodynamic levitation by melting the powders in a copper hearth. Structural transitions were monitored upon cooling from the melt to 1000 °C via in situ X-ray diffraction on aerodynamically levitated samples. The phase evolution was liquid, hexagonal H-type, and monoclinic B-type for composition 1 and liquid, cubic X-type, H-type, and B-type for composition 2. Based on their AIR, the general polymorphic transformations of the high-entropy RE_2O_3 follow the trend of single-RE RE_2O_3, but the transition temperatures differ from those of single-RE RE_2O_3. The coefficient of thermal expansion values of the B-type phase of compositions 1 and 2 are similar to those of Gd_2O_3 and previously published high-entropy RE_2O_3.

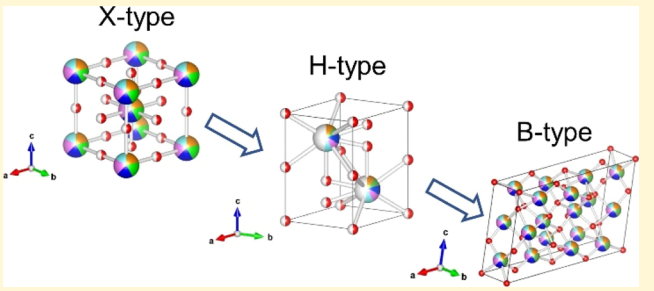

1. INTRODUCTION

Rare-earth (RE) sesquioxides (RE_2O_3) are of great technological importance due to their unique fundamental properties.[1] Typically, the oxides formed by the trivalent lanthanides from La^{3+} to Lu^{3+} and the RE-like Y^{3+} and Sc^{3+} cations are referred to as RE sesquioxides. Some of the RE_2O_3 offer a high quantum yield, attractive biocompatibility, high thermal and chemical stability, and resistance to phase transformation upon irradiation, which make them suitable for optical applications such as in white light and laser;[2] biomedical applications such as in drug delivery and cell tracking and labeling;[3] electronic applications such as electrochemical and electroluminescent sensors;[4] and radiation-resistant materials for application in reactors.[5,6] Complex mixtures of REs in sesquioxides may reveal attractive functional and structural properties that are still to be discovered.

Most of the RE_2O_3 undergo polymorphic transitions,[7] which should be considered when designing such materials for specific applications. Three structures are observed below 2000 °C: sesquioxides from La_2O_3 to Nd_2O_3 are stable with a trigonal structure (A-type, space group $P\bar{3}m1$); sesquioxides from Sm_2O_3 to Gd_2O_3 are stable with a monoclinic (B-type, $C2/m$) or cubic structure (C-type, $Ia\bar{3}$); Y_2O_3, Sc_2O_3, and sesquioxides from Tb_2O_3 to Lu_2O_3 are stable with a C-type structure. Above 2000 °C, sesquioxides from La_2O_3 to Tm_2O_3 transform into a high-temperature hexagonal structure (H-type, $P6_3/mmc$), and upon further heating sesquioxides from La_2O_3 to Eu_2O_3 transform into a cubic structure (X-type, $Im\bar{3}m$).[7,8] As an exception, sesquioxides formed by Yb, Lu, Y, and Sc maintain a single C-type structure from room temperature to melting.[7,8] A schematic diagram of polymorphic transformations for RE_2O_3 is shown in Figure 1. An additional orthorhombic perovskite ($Pnma$) structure is observed in $LaLuO_3$ and compounds with a similar difference in cationic radii.[9,10]

Mixing five or more REs in equiatomic amounts has been proven to result in single-phase RE_2O_3 with potential functional applications. Inspired by the compositional design of high-entropy oxides,[11,12] pioneering work on multicomponent RE oxides indicates the surprising stability of a single phase up to 1500 °C.[13,14] Such structural stability and the variety of high-entropy RE_2O_3 compounds that can be synthesized[15−19] open the door to the discovery of functional properties that may surpass the performance of single-RE oxides. A few properties reported for high-entropy RE oxides

Received: October 10, 2022
Revised: December 29, 2022
Published: January 13, 2023

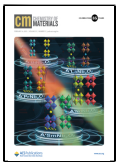

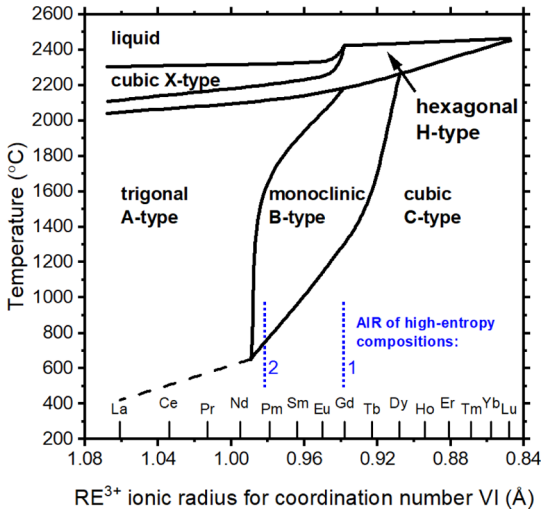

Figure 1. Schematic diagram of polymorphic transformations for single-RE RE_2O_3 as a function of temperature and RE ionic radius for coordination number VI.[8] Vertical dashed lines indicate the relative horizontal position of the AIR of compositions 1 $(Lu,Y,Ho,Nd,La)_2O_3$ and 2 $(Gd,Eu,Sm,Nd,La)_2O_3$.

include multiwavelength luminescence emission,[20] photocatalytic activity,[21] electrical conductivity,[22,23] and environmental barrier coating.[24]

Only a few studies focus on the polymorphic transformations and thermal expansion of high-entropy RE_2O_3 at elevated temperatures. Such knowledge is relevant for applications and synthesis methods that involve refractory temperatures such as environmental barrier coating and crystal growth from the melt, respectively. A single C-type phase was reported for $(Gd,Tb,Dy,Ho,Er)_2O_3$ up to 1650 °C.[16] However, one might expect a transition to H- and/or X-type phases around 2000 °C as in the case of single-RE RE_2O_3. In fact, another report demonstrates the transition sequence B-, H-, and X-type in the range 1900−2400 °C for $(La,Sm,Dy,Er,X)_2O_3$, where X is either Nd, Gd, or Y.[17] The reported coefficient of thermal expansion (CTE) of these compounds is similar to that of Gd_2O_3.[25] However, it is not yet clear how composition affects the polymorphic behavior and thermal expansion of high-entropy RE_2O_3.

Since the polymorphism of single-RE RE_2O_3 is dictated by the RE^{3+} ionic radius,[8] the average ionic radius (AIR) of complex compositions may play an important role in their structural stability. To investigate that, we designed two five-component, equiatomic sesquioxide compositions. Composition 1 $(Lu,Y,Ho,Nd,La)_2O_3$ has a medium AIR (0.938 Å) that was achieved by mixing small (Lu^{3+}, Y^{3+}, and Ho^{3+}) and large cations (Nd^{3+} and La^{3+}). The AIR of composition 1 is equal to the ionic radius of Gd^{3+} although Gd^{3+} is not included in the composition. With composition 1, we investigate whether the polymorphism of the high-entropy sesquioxide will be similar to that of Gd_2O_3. Composition 2 $(Gd,Eu,Sm,Nd,La)_2O_3$ has a medium AIR (0.982 Å) that was achieved by mixing medium (Gd^{3+}, Eu^{3+}, and Sm^{3+}) and large cations (Nd^{3+} and La^{3+}). The AIR of composition 2 is close to that of medium-sized Pm^{3+} (0.982 Å) although Pm^{3+} is not included in the composition. With composition 2, we investigate whether the polymorphism of Pm_2O_3 can be replicated in a high-entropy sesquioxide without including the unstable Pm isotopes in the compound. The structural evolution of both compounds is analyzed upon cooling from the melt via in situ high-temperature X-ray diffraction (XRD) in the range of 1000−2450 °C. The unique sample aerodynamic levitation capability allowed data collection at extreme temperatures (>2400 °C) in a containerless sample environment.

2. METHODS

2.1. Composition Formulation. To study the effect of AIR on the polymorphic behavior of high-entropy RE_2O_3, two five-component equiatomic compositions were formulated. The criterion to select RE elements was their ionic radii. Composition 1 $(Lu,Y,Ho,Nd,La)_2O_3$ contains a mixture of small (Lu^{3+}, Y^{3+}, and Ho^{3+}) and large (Nd^{3+} and La^{3+}) REs, and composition 2 $(Gd,Eu,Sm,Nd,La)_2O_3$ contains a mixture of medium (Gd^{3+}, Eu^{3+}, and Sm^{3+}) and large REs; commas in sample composition indicate equiatomic amounts. Table 1 shows a list of REs and their respective ionic radius; the AIR of compositions 1 and 2 are included for comparison. The AIR of composition 1 is the same as the ionic radius of Gd^{3+}, while the AIR of composition 2 is close to that of Pm^{3+} (0.979 Å), although Pm was not included in any of the two formulations.[26]

2.2. Synthesis of Precursor Powder Samples. Powder samples were prepared using a wet chemistry synthesis method. RE nitrates $RE(NO_3)_3{\cdot}xH_2O$ of 99.99% purity were used as the source of cations. A list of nitrates used are seen in Table 2. The powders were calcined in air at 550 °C for 2.5 h, and finally, crystallized in air at 900 °C for 1 h. These powders were used as a precursor material for the preparation of spherical bead samples as described in Section 2.4.

2.3. Room-Temperature Powder XRD. To determine the structure of the as-prepared powders, the samples were subjected to room-temperature powder XRD. A PANalytical Empyrean diffractometer was used in Bragg−Brentano geometry. X-rays were generated from a Cu Kα source operated at 45 kV and 40 mA. The following optics were used on the incident X-ray beam: 0.04 rad Soller slits, a 1/4° divergence slit, a 10 mm fixed-beam mask, and a 1/2° antiscatter slit. The following optics were used on the diffracted X-ray beam: a 1/4° antiscatter slit, 0.04 rad Soller slits, and a nickel β filter. A PIXcel^{3D} detector was used to collect the diffraction patterns. Patterns were collected in the 2θ range of 20−90°. The General Structure Analysis System II software (GSAS-II) was used to perform Rietveld structure refinements[27] and obtain phase composition and lattice parameters.

Table 1. List of RE^{3+} Cations, Their Respective Ionic Radius, and the AIR of High-Entropy Compositions 1 and 2 for Coordination Number VI[26a]

	RE^{3+} cations								
	Lu^{3+}	Y^{3+}	Ho^{3+}	Gd^{3+}	Eu^{3+}	Sm^{3+}	Pm^{3+}	Nd^{3+}	La
ionic radius (Å)	0.848	0.892	0.894	0.938	0.950	0.964	0.979	0.995	1.061
		sample ID and composition							
		1 $(Lu,Y,Ho,Nd,La)_2O_3$					2 $(Gd,Eu,Sm,Nd,La)_2O_3$		
AIR (Å)		0.938					0.982		

[a]Commas in sample compositions indicate equiatomic amounts.

https://doi.org/10.1021/acs.chemmater.2c03088
Chem. Mater. 2023, 35, 1116−1124

Table 2. Composition, Manufacturer, and Purity of Nitrate Used in the Synthesis of Precursor Powder

nitrate	composition	supplier	purity (%)
lutetium nitrate hydrate	$Lu(NO_3)_3{\cdot}6H_2O$	Thermo Scientific	99.99
yttrium nitrate hydrate	$Y(NO_3)_3{\cdot}4H_2O$	Sigma-Aldrich	99.99
holmium nitrate hydrate	$Ho(NO_3)_3{\cdot}5H_2O$	Alfa Aesar	99.99
gadolinium nitrate hydrate	$Gd(NO_3)_3{\cdot}6H_2O$	Sigma-Aldrich	99.99
europium nitrate hydrate	$Eu(NO_3)_3{\cdot}6H_2O$	Alfa Aesar	99.99
samarium nitrate hydrate	$Sm(NO_3)_3{\cdot}6H_2O$	Alfa Aesar	99.99
neodymium nitrate hydrate	$Nd(NO_3)_3{\cdot}6H_2O$	Alfa Aesar	99.99
lanthanum nitrate hydrate	$La(NO_3)_3{\cdot}6H_2O$	Sigma-Aldrich	99.99

2.4. Preparation of Spherical Bead Samples for In Situ High-Temperature Diffraction Experiments. The precursor powder samples described in Section 2.3 were melted in a copper hearth to prepare 2- to 3-mm-diameter spherical samples. Herein, such spherical samples are referred to as beads. A 400 W continuous-wave CO_2 laser was used to heat and melt the powders. The melt was rapidly cooled by turning off the laser so that the samples maintained a spherical shape. The bead samples have a favorable sample geometry for subsequent aerodynamic levitation during the in situ high-temperature diffraction experiments described in Section 2.5. The preparation of bead samples was performed at the Spallation Neutron Source at Oak Ridge National Laboratory (ORNL).

2.5. Structural Evolution Analysis with In Situ High-Temperature XRD. The bead samples were used to study the polymorphic behavior of both 1 $(Lu,Y,Ho,Nd,La)_2O_3$ and 2 $(Gd,Eu,Sm,Nd,La)_2O_3$ via in situ high-temperature synchrotron-generated XRD at the Advanced Photon Source (APS), beamline 6-ID-D, at Argonne National Laboratory (ANL). To achieve elevated temperatures (>2400 °C) without concern with sample holder stability and reactivity, a containerless sample environment was adopted by using an aerodynamic conical nozzle levitator system.[28] Bead samples were placed on the levitator nozzle, and ultrahigh-purity Ar gas was used to levitate the samples. The vertical position of the levitator was adjusted with respect to the X-ray beam to provide diffraction from the top part of the sample. Monochromatic synchrotron radiation (0.124035 Å) was used to obtain diffraction patterns in the Debye−Scherrer geometry. An amorphous silicon 2D X-ray detector was used, and the sample-to-detector distance was ∼1241 mm. Room-temperature diffraction from a LaB_6 standard sample was obtained to calibrate the detector distance and tilt.

To heat the samples, a Synrad Firestar i401 400 W continuous-wave CO_2 laser (10.6 μm) was focused on the top of the beads. A Chino IR-CAS near-infrared optical pyrometer was used to record the sample temperature, which was estimated using Wien's law. The emissivity of the samples was set to 0.92, which is a typical value for oxides.[29] Both laser and X-ray beams were co-incident on the top few hundred microns of the sample. The experimental setup used in this work has been thoroughly described before.[30−32] The mass change of the bead samples after the data collection was lower than 1.3 wt %.

Diffraction patterns were collected upon cooling the samples from the melt. A room-temperature pattern was initially collected and then the samples were melted. The FIT2D software was used for real-time visualization of the diffraction patterns; the molten state was determined when the diffraction lines were no longer seen, and a typical pattern from a liquid sample was observed.[33] Diffraction patterns were obtained at constant temperatures every 50 °C down to 1000 °C; the cooling rate between temperature steps was ∼20 °C/min. FIT2D was used to refine instrumental parameters and integrate the 2D diffraction images into 1D patterns. GSAS II was used for Rietveld structure refinement.

3. RESULTS AND DISCUSSION

3.1. Structure of As-Prepared Powders. A single C-type phase was observed for as-prepared powders of compositions 1 and 2. As seen in Figure 2, the room-temperature powder XRD

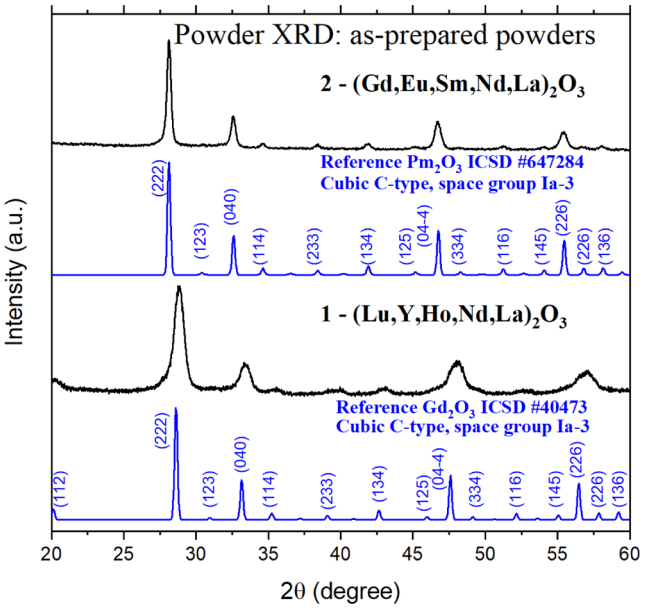

Figure 2. Room-temperature powder XRD patterns of the as-prepared powders. Samples of compositions 1 and 2 have a single C-type phase. Reference patterns of C-type Gd_2O_3 (ICSD no. 40473) and Pm_2O_3 (ICSD no. 647284) are included for comparison.

patterns of compositions 1 and 2 match well with reference patterns of C-type Gd_2O_3 and Pm_2O_3, respectively, which is expected since the AIR of the high-entropy compounds is close to the ionic radii of Gd^{3+} and Pm^{3+} as seen in Table 1. At 900 °C, which is the highest temperature to which powders were heated during the synthesis, the expected structure of compositions 1 and 2 should be the C- and B-type, respectively, considering their AIR in the schematic diagram of polymorphic transformations seen in Figure 1. Considering that the C- to B-type transition is irreversible in single-RE RE_2O_3,[7] composition 2 may have this transition above 900 °C, which is surprising since the transition occurs at 700 °C for Pm_2O_3.[34] This indicates that the complex nature of composition 2 favors the C-type structure over a wide range of temperatures compared to single-RE RE_2O_3 of similar AIR. Significant variations in phase-transition temperatures of high-entropy RE_2O_3 compared to single-RE RE_2O_3 have been previously reported.[17] Therefore, polymorphic transition temperatures of high-entropy RE_2O_3 cannot be predicted by the diagram of polymorphic transformations of single-RE RE_2O_3.

The powder of composition 1 has a more intense lattice strain and a smaller unit cell volume than composition 2. In Figure 2, the more pronounced peak broadening observed for composition 1 indicates a more intense lattice strain. This is expected since composition 1 combines small and large RE^{3+} and this disparity in ionic radii induces lattice strain. The refined lattice parameters of compositions 1 and 2 are 10.7313 and 10.9950 Å, respectively. Therefore, composition 2 has a larger C-type unit cell, which is expected since composition 2 is composed of larger REs as seen in Table 1.

https://doi.org/10.1021/acs.chemmater.2c03088
Chem. Mater. 2023, 35, 1116−1124

3.2. Structure of the As-Prepared Bead Samples. A single monoclinic B-type structure was observed for the as-prepared beads of compositions 1 $(Lu,Y,Ho,Nd,La)_2O_3$ and 2 $(Gd,Eu,Sm,Nd,La)_2O_3$, indicating a phase transition from the C-type phase seen in the powders. Room-temperature synchrotron XRD patterns of the as-prepared beads were obtained on the conical nozzle levitator setup prior to the high-temperature experiments. Figure 3 includes those patterns with

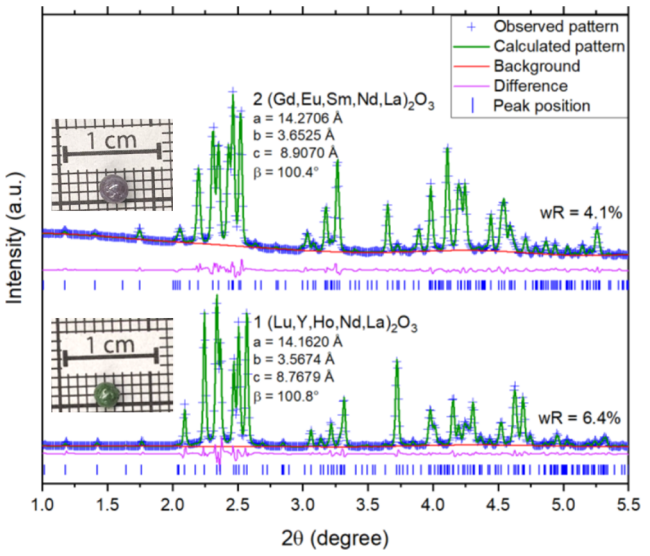

Figure 3. Room-temperature synchrotron XRD patterns and Rietveld refinement results of the as-prepared beads of compositions 1 $(Lu,Y,Ho,Nd,La)_2O_3$ and 2 $(Gd,Eu,Sm,Nd,La)_2O_3$. Both compounds have a single B-type phase. The lattice parameters of the monoclinic unit cell are listed in the figure.

Rietveld refinement results. The patterns of both samples were well fitted with calculated patterns of a single monoclinic phase. As seen from the lattice parameters listed in Figure 3, the bead of composition 1 has a smaller unit cell volume (434.996 $Å^3$) than that of composition 2 (456.632 $Å^3$), which is expected considering their AIR listed in Table 1. Since the beads were prepared by melting the powders with a C-type phase, there is a phase transition from C- to B-type for both compositions 1 and 2. In this work, high-temperature phase transitions are determined using the bead samples; therefore, the C- to B-type transition temperature is not investigated.

3.3. Phase Evolution upon Cooling from the Melt. *3.3.1. Phase Evolution of Composition 1 $(Lu,Y,Ho,Nd,La)_2O_3$.* As the bead of composition 1 was cooled from the melt, XRD patterns corresponding to liquid, single H-type phase, and single B-type phase were observed as seen in Figure 4. Rietveld refinement results are listed in Table S1 in the Supporting Information. A schematic representation of the phase evolution is shown in Figure 5, left. The sample of composition 1

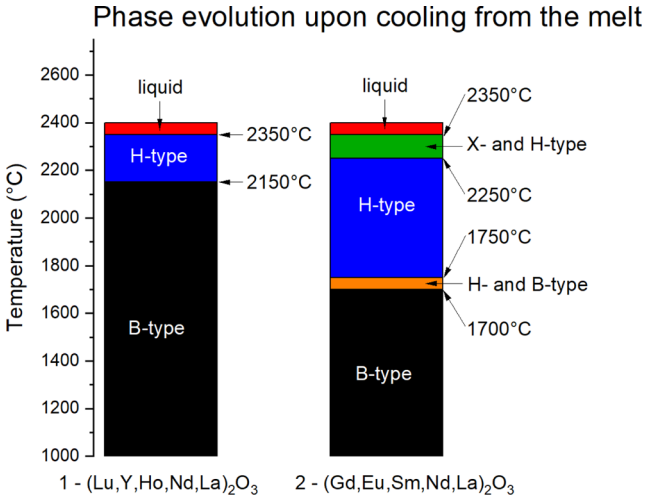

Figure 5. Schematic representation of phase transitions observed upon cooling from the melt for compositions 1 (left) and 2 (right).

solidified at ~2350 °C with a single H-type structure. A transition from single H-type to a single B-type structure occurred at ~2150 °C. None of the diffraction patterns indicated a mixture of H- and B-type phases. Therefore, it is likely that the thermal equilibrium between both phases occurs between 2200 °C (single H-type phase) and 2150 °C (single B-type phase), which correspond to the temperatures of consecutive measurements. The B-type phase was stable upon

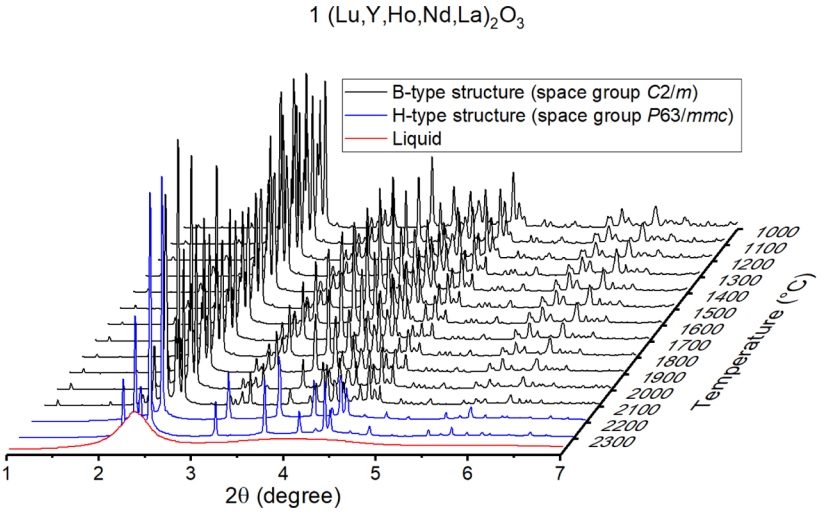

Figure 4. In situ high-temperature XRD patterns of composition 1 $(Lu,Y,Ho,Nd,La)_2O_3$. The transitions observed upon cooling from the melt are liquid to H-type (~2350 °C) and H-type to B-type (~2150 °C).

https://doi.org/10.1021/acs.chemmater.2c03088
Chem. Mater. 2023, 35, 1116−1124

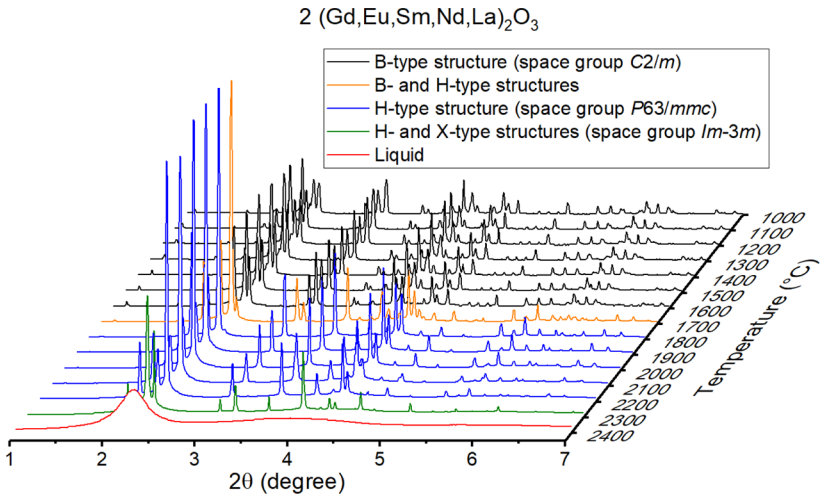

Figure 6. In situ high-temperature XRD patterns of composition 2 $(Lu,Y,Ho,Nd,La)_2O_3$. The transitions observed upon cooling from the melt are liquid to a mixture of H- and X-type structures (~2350 °C), a single H-type (2250 °C), a mixture of B- and H-type structures (1750 °C), and a single B-type structure (1700 °C).

cooling to 1000 °C. These polymorphic transformations are expected according to the position of the AIR of composition 1 in the diagram of polymorphic transformations in Figure 1. The transition temperatures listed here correspond to the temperature at which a diffraction pattern indicated a different crystal structure than the immediately preceding collected pattern. Exact phase-transition temperatures may lie within the 50 °C temperature step between measurements.

Both the melting and B- to H-type transition temperatures of composition 1 are close to the smaller end of the temperature range previously reported for Gd_2O_3. Composition 1 is compared to Gd_2O_3 because its AIR is the same as the ionic radius of Gd^{3+}, Table 1. The melting point of Gd_2O_3 is reported in the range of 2392−2445 °C[35−40] while composition 1 solidifies ~2350 °C. This is in agreement with previous work that demonstrated that the melting point of RE_2O_3 can be suppressed in high-entropy compositions with similar AIR.[41] The B- to H-type transition temperature of Gd_2O_3 is reported in the range of 2170−2195 °C,[36,39] while composition 1 had this transition at ~2150 °C, which is close to the lower end of this range. Therefore, the polymorphic behavior of single-RE_2O_3 can be used to predict the type of phase transformations that may occur in high-entropy RE_2O_3.

3.3.2. Phase Evolution of composition 2 $(Gd,Eu,Sm,Nd,La)_2O_3$. As the bead of composition 2 was cooled from the melt, XRD patterns corresponding to liquid, a mixture of X- and H-type, single H-type, a mixture of H- and B-type, and single H-type structures were observed as seen in Figure 6. Rietveld refinement results are listed in Table S2 in the Supporting Information. A schematic representation of the phase evolution is shown in Figure 5, right. The sample of composition 2 solidified at ~2350 °C, and a mixture of H- and X-type structures was observed at ~2350 and ~2300 °C; the relative amounts of the H-type phase were 57 and 95 wt %, respectively. This indicates that the cubic X-type phase is stable in a relatively short temperature range, and the H-type phase is preferentially formed at temperatures close to the melting point. A single H-type phase was observed from 2250 to 1800 °C. The H- to B-type transition was observed at 1750 °C with a mixture of both phases (81 wt % H-type). Upon further cooling, a single B-type phase was observed from 1700 to 1000 °C.

The observed polymorphic transformations of composition 2 are slightly different than the ones predicted in the diagram of polymorphic transformations in Figure 1 for the respective AIR. Since the AIR of composition 2 is close to that of Pm^{3+}, the polymorphism of Pm_2O_3 will be considered to compare to composition 2. The melting point of Pm_2O_3 (X-type to liquid) was reported as 2320 °C,[34,40] while composition 2 solidifies at ~2350 °C. The X- to H-type transition of Pm_2O_3 was reported at 2225 °C,[34,40] indicating that the temperature range of stability of the X-type structure is larger for Pm_2O_3 (~100 °C) than composition 2, for which a single X-type phase was not observed. Additionally, the H- to A-type transition was reported for Pm_2O_3 in the range of 2117−2135 °C[34,40] but was not observed for composition 2. Finally, the A- to B-type transition of Pm_2O_3 was reported in the range of 1600−1740 °C,[34,42] while the H- to B-type transition was observed at 1750 °C which is close to the larger end of the reported range. Once again, the polymorphic behavior of a high-entropy RE_2O_3 could not be accurately predicted by the polymorphism of a single-RE RE_2O_3 with a similar AIR.

The surprising H- to B-type phase transition without an intermediate A-type phase was supported by Rietveld refinement but was not expected based on the AIR of composition 2 and the phase diagram in Figure 1. Figures S1 and S2 in the Supporting Information are the observed data and refinement results for the diffraction patterns collected at 1800 °C (single H-type phase, weighted R factor wR = 8.1%) and 1700 °C (single B-type phase, wR = 6.0%). Figure S3 shows the diffraction pattern collected at 1750 °C; the most intense peaks correspond to the H-type phase, while secondary phase peaks are well-fitted for the B-type structure with a wR = 4.3%. In Figure S4, an attempt to refine a mixture of H- and A-type phases for this same pattern collected at 1750 °C does not fit the secondary peaks and results in a wR = 19.9%. Therefore, an intermediate A-type structure between the H- to B-type transformation was not detected in this study.

In general, the polymorphic nature of both compositions 1 and 2 as a function of their AIR is in agreement with the polymorphism of single-RE RE_2O_3 as seen in Figures 1 and 5. Upon cooling from the melt, the transition sequence for the smaller-AIR composition 1 was liquid, H-type, and B-type structure, while for the larger-AIR composition 2, the sequence

https://doi.org/10.1021/acs.chemmater.2c03088
Chem. Mater. 2023, 35, 1116−1124

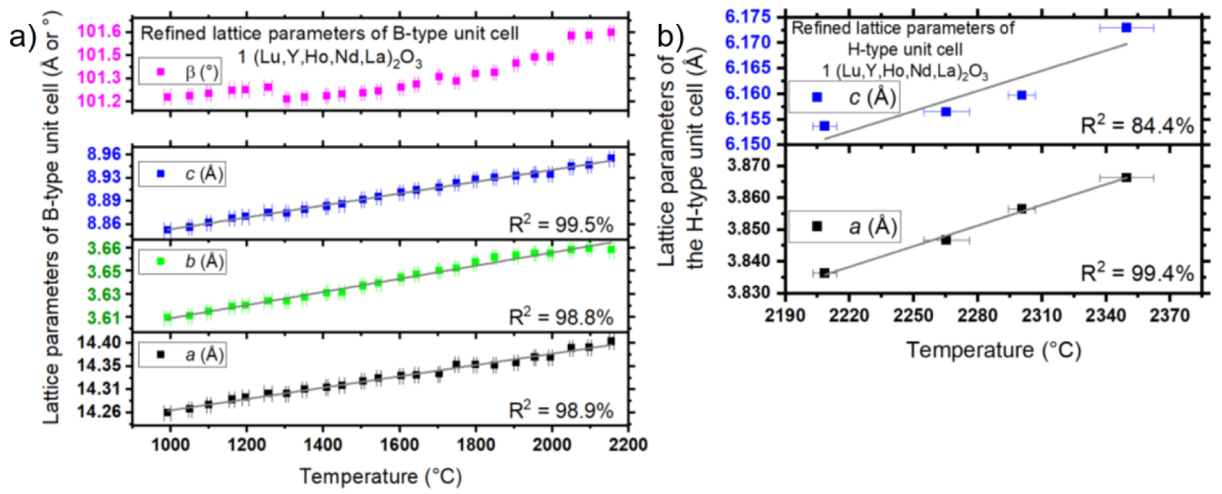

Figure 7. Lattice parameters of B-type (a) and H-type (b) structures of composition 1 $(Lu,Y,Ho,Nd,La)_2O_3$. Values were obtained from Rietveld structure refinement using in situ high-temperature XRD data. Gray lines are linear regression fittings, and their respective goodness-of-fit R^2 is included in the images.

Table 3. CTE for Each Lattice Axis of B- or H-Type Unit Cells for Compositions 1 and 2 as Well as Literature Values for B-Type Gd_2O_3 and $(La,Sm,Dy,Er,X)_2O_3$, Where X = Nd, Gd, or Y[a]

			CTE α ($\times 10^{-6}$/K)			
sample	phase	temperature range (°C)	α_a(*a*-axis)	α_b(*b*-axis)	α_c(*c*-axis)	*A* ($\times 10^{-6}$/K)
1 $(Lu,Y,Ho,Nd,La)_2O_3$	B-type	1000−2150	7.8 ± 0.2	13.4 ± 0.3	10.5 ± 0.2	11
2 $(Gd.Eu,Sm,Nd,La)_2O_3$	B-type	1000−1700	9.0 ± 0.3	18.8 ± 0.3	13.2 ± 0.2	19
	H-type	1800−2250	41 ± 3		32 ± 1	18
Gd_2O_3 from ref 25	B-type	20−900	9.7 ± 0.2	15.4 ± 0.4	13.9 ± 0.2	11
$(La,Sm,Dy,Er,X)_2O_3$; X = Nd, Gd, or Y from ref 17	B-type	25−∼1950	7.8 ± 0.7	16 ± 2	12 ± 5	16

[a]Anisotropic factor (A) values are included.

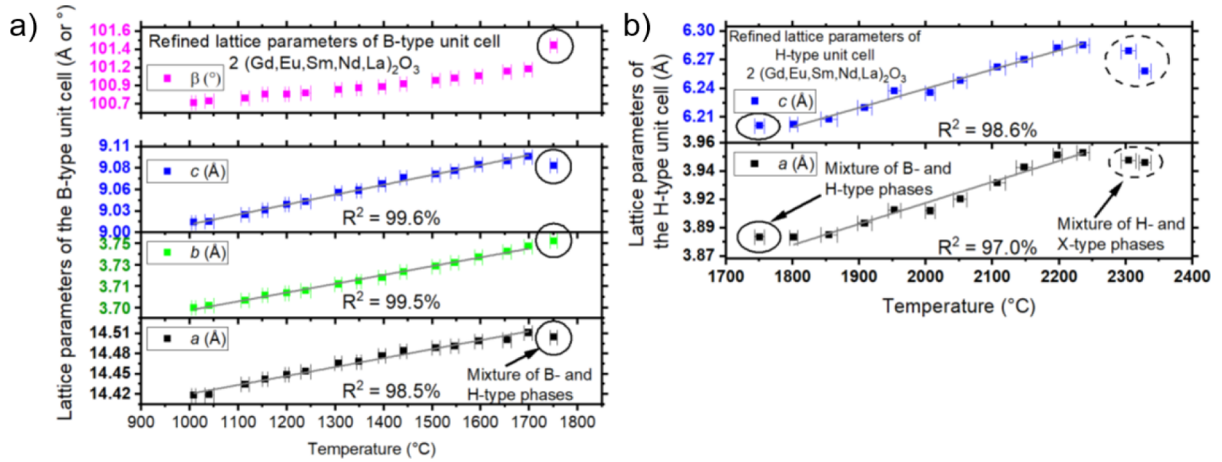

Figure 8. Lattice parameters of B-type (a) and H-type (b) structures of composition 2 $(Gd,Eu,Sm,Nd,La)_2O_3$. Values were obtained from Rietveld structure refinement using the in situ high-temperature XRD data. Gray lines are linear regression fittings, and their respective goodness-of-fit R^2 is included in the images.

was liquid, X-type, H-type, and B-type. Additionally, the transition to a B-type phase was at a much lower temperature for composition 2 (1700 °C) than for composition 1 (2150 °C). It is important to note that the specific transition temperatures of compositions 1 and 2 could not be predicted by the diagram in Figure 1. Also, composition 2 did not form the A-type phase indicated in that diagram.

3.4. Thermal Expansion Coefficient Obtained from Refined Unit Cell Parameters. *3.4.1. Thermal Expansion of Composition 1 $(Lu,Y,Ho,Nd,La)_2O_3$.* Structure refinement results indicate the expansion of B- and H-type unit cells with increasing temperature for composition 1. Figure 7a includes the lattice parameters *a*, *b*, *c*, and β of the B-type unit cell. The parameter β corresponds to the angle formed between the *a*- and *c*-axes. The discontinuity in β values with temperature in Figure 7a is insignificant if two factors are taken into account: (1) the β values varied less than 0.5% in the entire temperature range (from ∼101.2 to 101.6°) and (2) the standard deviation of β values obtained from Rietveld refinement is ∼0.05°. Figure 7b includes the lattice parameters

https://doi.org/10.1021/acs.chemmater.2c03088
Chem. Mater. 2023, 35, 1116−1124

a and c of the H-type unit cell. A relatively low goodness-of-fit R^2 (84.4%) was obtained for the linear regression of the H-type lattice parameter c. This deviation from linearity is not statistically significant because only four data points are available for the H-type cell.

Refined lattice parameters can be used to determine the high-temperature CTE. The CTE α is determined as

$$\alpha = \left(\frac{\mathrm{d}l}{\mathrm{d}T}\right)\frac{1}{l_0} \quad (1)$$

where l is the lattice parameter and T is the temperature. The differential expression $\mathrm{d}l/\mathrm{d}T$ was taken as the slope of the linear regression applied to the lattice parameter data (Figure 7a). Additionally, l_0 was taken as the refined lattice parameter at the lowest temperature that a given crystal structure was observed during the high-temperature experiments. The CTE values of the B-type phase of composition 1 are listed in Table 3.

Composition 1 has CTE values similar to those of Gd_2O_3 and previously published high-entropy RE_2O_3. Sawbridge and Waterman[25] reported the CTE of B-type Gd_2O_3 in the range of 20−900 °C, and Ushakov et al.[17] reported the CTE of B-type $(La,Sm,Dy,Er,X)_2O_3$, where X is either Nd, Gd, or Y from room temperature to ∼1950 °C. The reported values are in Table 3; the $(La,Sm,Dy,Er,X)_2O_3$ compounds had similar CTE, and only one set of values is listed. The similarity in the CTE values of composition 1, Gd_2O_3, and $(La,Sm,Dy,Er,X)_2O_3$ indicates that complex compositions do not largely affect the thermal expansion of RE_2O_3. It is not possible to accurately calculate the CTE of the H-type structure for composition 1 because of its narrow temperature range of stability and the resulting small number of data points seen in Figure 7b.

3.4.2. Thermal Expansion of Composition 2 $(Gd,Sm,Eu,Nd,La)_2O_3$. Structure refinement results indicate the expansion of the B- and H-type unit cell with temperature for composition 2. Figure 8a includes the lattice parameters a, b, c, and β of the B-type unit cell. The angle β varied less than 1% in the entire temperature range in which the B-type phase was observed. At 1750 °C, a mixture of B- and H-type phases was observed. At this temperature, the lattice parameters a and c of the B-type unit cell lie below the linear trend seen for the values obtained at lower temperatures. This indicates that the B-type cell is richer in smaller REs than the H-type cell at 1750 °C. A similar observation is seen at ∼2300 and 2350 °C in Figure 8b. At those temperatures, there is a mixture of H- and X-type phases, and the H-type phase is richer in smaller REs than the X-type phase. Such deviation from linearity for lattice parameter values at phase-transition temperatures is a common phenomenon.[43−45] The X-type phase was observed in only two diffraction patterns, and its lattice parameter increased from 4.37397 Å at ∼2300 °C to 4.3807 Å at ∼2350 °C.

For composition 2, the CTE values of the H-type phase are significantly larger than those of the B-type phase as seen in Table 3. The B-type phase has CTE values similar to those of composition 1, which suggests that the type of REs in a high-entropy sesquioxide does not largely affect the CTE. A relatively large number of lattice parameter data points allowed the calculation of the CTE values of the H-type phase of composition 2 seen in Table 3. To the best of our knowledge, the CTE of H-type single-RE or high-entropy RE_2O_3 has not been previously reported. The CTE of the hexagonal $YbFeO_3$ (same space group as the B-type structure, $C2/m$) along the c-axis was reported as $\sim 30 \times 10^{-6}$/K,[46] which is similar to the calculated value for composition 2 seen in Table 3. It is important to mention that the CTE calculations reported here did not include the lattice parameters corresponding to temperatures at which a mixture of phases was observed (1750, 2300, and 2350 °C).

Composition 2 has a higher degree of expansion anisotropy than composition 1 and is less favorable for high-temperature applications and synthesis methods. The anisotropic factor A is given by $A = |\alpha_a - \alpha_b| + |\alpha_a - \alpha_c| + |\alpha_b - \alpha_c|$ and is listed in Table 3. High A values for composition 2 indicate a greater disparity in the CTE along the unit cell axes, which makes it more likely to fracture if subjected to high-temperature applications under cycling conditions. Additionally, materials with high A values are more challenging to be grown as single crystals via directional solidification. As the crystal cools, twinning and cracking may result from the expansion anisotropy and are more likely to occur for materials with high A values.[47,48]

4. CONCLUSIONS

The polymorphic structures formed in high-entropy RE_2O_3 are dictated by their AIR and follow the general trend of single-RE RE_2O_3. Upon cooling from the melt to 1000 °C, the phase evolution observed for composition 1 $(Lu,Y,Ho,Nd,La)_2O_3$ was liquid, H-type, and B-type. The AIR of composition 1 is equal to that of Gd^{3+}, its polymorphic behavior is similar to that of Gd_2O_3, and the transition temperatures are lower for the high-entropy compound. The phase evolution observed for composition 2 $(Gd,Eu,Sm,Nd,La)_2O_3$ was liquid, X-type, H-type, and B-type. The AIR of composition 2 is close to that of Pm^{3+}; however, the polymorphic behavior of the high-entropy sesquioxide could not be predicted by the polymorphism of Pm_2O_3 because no H- to A-type transition was detected. Additionally, the X-type phase is stable in a much shorter temperature range for composition 2 than Pm_2O_3.

Complex compositions do not largely affect the CTE of the B-type phase; the CTE of the H-type phase was reported for the first time and is considerably larger than that of the B-type phase. Both compositions 1 and 2 have CTE values that are similar to those of Gd_2O_3 and previously published high-entropy RE_2O_3. The CTE of the B-type phase is α_a, α_b, and α_c equal to 7.8, 13.4, and 10.5×10^{-6}/K for composition 1, and 9.0, 18.8, and 13.2×10^{-6}/K for composition 2, respectively. For the first time, we report the CTE values of the H-type phase of a RE_2O_3, which are significantly larger than those of the B-type phase. Composition 2 has α_a and α_c equal to 41 and 32×10^{-6}/K, respectively.

Future investigation of high-temperature applications and synthesis methods for high-entropy RE_2O_3 can benefit from the polymorphism and thermal expansion results reported here. Novel compounds could be tailored as a function of AIR to prioritize a specific structure over a desired temperature range or to adjust transition temperatures. Additionally, RE combinations other than the ones reported here may result in compounds with surprisingly different polymorphic and thermal expansion behaviors, which inspire further investigation.

https://doi.org/10.1021/acs.chemmater.2c03088
Chem. Mater. 2023, 35, 1116−1124

■ ASSOCIATED CONTENT

Supporting Information

The Supporting Information is available free of charge at https://pubs.acs.org/doi/10.1021/acs.chemmater.2c03088.

Rietveld structure refinement results for samples 1 $(Lu,Y,Ho,Nd,La)_2O_3$ and 2 $(Gd,Eu,Sm,Nd,La)_2O_3$ obtained from in situ high-temperature XRD and structure refinement images indicating the absence of the A-type phase in sample 2 (PDF)

■ AUTHOR INFORMATION

Corresponding Author

Matheus Pianassola − *Scintillation Materials Research Center and Department of Materials Science and Engineering, University of Tennessee, Knoxville, Tennessee 37996, United States;* orcid.org/0000-0001-7468-2794; Email: mpianass@utk.edu

Authors

Kaden Anderson − *Scintillation Materials Research Center and Department of Materials Science and Engineering, University of Tennessee, Knoxville, Tennessee 37996, United States*

Can Agca − *Materials Science and Technology Division, Oak Ridge National Laboratory, Oak Ridge, Tennessee 37831, United States;* orcid.org/0000-0003-1427-7812

Chris J. Benmore − *X-Ray Science Division, Advanced Photon Source, Argonne National Laboratory, Argonne, Illinois 60439, United States*

Jake W. McMurray − *Materials Science and Technology Division, Oak Ridge National Laboratory, Oak Ridge, Tennessee 37831, United States*

Jöerg C. Neuefeind − *Neutron Scattering Division, Oak Ridge National Laboratory, Oak Ridge, Tennessee 37831, United States*

Charles Melcher − *Scintillation Materials Research Center and Department of Materials Science and Engineering, University of Tennessee, Knoxville, Tennessee 37996, United States; Department of Nuclear Engineering, University of Tennessee Knoxville, Knoxville, Tennessee 37996, United States*

Mariya Zhuravleva − *Scintillation Materials Research Center and Department of Materials Science and Engineering, University of Tennessee, Knoxville, Tennessee 37996, United States*

Complete contact information is available at: https://pubs.acs.org/10.1021/acs.chemmater.2c03088

Notes

The authors declare no competing financial interest.

■ ACKNOWLEDGMENTS

This work was supported by the National Science Foundation (DMR 1846935). This material is partially based upon work supported by the U.S. Department of Homeland Security under grant award number 20CWDARI00037-01-00. The views and conclusions contained in this document are those of the authors and should not be interpreted as necessarily representing the official policies, either expressed or implied, of the U.S. Department of Homeland Security. Powder XRD was performed at the Institute for Advanced Materials & Manufacturing (IAMM) Diffraction Facility, located at the University of Tennessee, Knoxville. A portion of this research used resources at the Spallation Neutron Source, a DOE Office of Science User Facility operated by the Oak Ridge National Laboratory. Use of the Advanced Photon Source, an Office of Science User Facility operated for the U.S. Department of Energy (DOE) Office of Science by Argonne National Laboratory, was supported by the U.S. DOE under contract no. DE-AC02-06CH11357.

■ REFERENCES

(1) *Binary Rare Earth Oxides*; Adachi, G., Imanaka, N., Kang, Z. C., Eds.; Springer Netherlands, 2004.

(2) Hossain, M. K.; Hossain, S.; Ahmed, M. H.; Khan, M. I.; Haque, N.; Raihan, G. A. A Review on Optical Applications, Prospects, and Challenges of Rare-Earth Oxides. *ACS Appl. Electron. Mater.* **2021**, *3*, 3715−3746.

(3) Hossain, M. K.; Khan, M. I.; El-Denglawey, A. A Review on Biomedical Applications, Prospects, and Challenges of Rare Earth Oxides. *Appl. Mater. Today* **2021**, *24*, 101104.

(4) Hossain, M. K.; Ahmed, M. H.; Khan, M. I.; Miah, M. S.; Hossain, S. Recent Progress of Rare Earth Oxides for Sensor, Detector, and Electronic Device Applications: A Review. *ACS Appl. Electron. Mater.* **2021**, *3*, 4255−4283.

(5) Pavlik, A., III; Ushakov, S. V.; Navrotsky, A.; Benmore, C. J.; Weber, R. J. K. Structure and Thermal Expansion of Lu2O3 and Yb2O3 up to the Melting Points. *J. Nucl. Mater.* **2017**, *495*, 385−391.

(6) Tracy, C. L.; Lang, M.; Zhang, F.; Trautmann, C.; Ewing, R. C. Phase transformations inLn2O3materials irradiated with swift heavy ions. *Phys. Rev. B: Condens. Matter Mater. Phys.* **2015**, *92*, 174101.

(7) Zhang, Y.; Jung, I. H. Critical Evaluation of Thermodynamic Properties of Rare Earth Sesquioxides (RE = La, Ce, Pr, Nd, Pm, Sm, Eu, Gd, Tb, Dy, Ho, Er, Tm, Yb, Lu, Sc and Y). *Calphad* **2017**, *58*, 169−203.

(8) Adachi, G. Y.; Imanaka, N. The Binary Rare Earth Oxides. *Chem. Rev.* **1998**, *98*, 1479−1514.

(9) Ovanesyan, K. L.; Petrosyan, A. G.; Shirinyan, G. O.; Pedrini, C.; Zhang, L. Single Crystal Growth and Characterization of LaLuO3. *Opt. Mater.* **1998**, *10*, 291−295.

(10) Ito, K.; Tezuka, K.; Hinatsu, Y. Preparation, Magnetic Susceptibility, and Specific Heat on Interlanthanide Perovskites ABO3 (A=La−Nd, B=Dy−Lu). *J. Solid State Chem.* **2001**, *157*, 173−179.

(11) Rost, C. M.; Sachet, E.; Borman, T.; Moballegh, A.; Dickey, E. C.; Hou, D.; Jones, J. L.; Curtarolo, S.; Maria, J.-P. Entropy-Stabilized Oxides. *Nat. Commun.* **2015**, *6*, 8485.

(12) Musicó, B. L.; Gilbert, D.; Ward, T. Z.; Page, K.; George, E.; Yan, J.; Mandrus, D.; Keppens, V. The Emergent Field of High Entropy Oxides: Design, Prospects, Challenges, and Opportunities for Tailoring Material Properties. *APL Mater.* **2020**, *8*, 040912.

(13) Djenadic, R.; Sarkar, A.; Clemens, O.; Loho, C.; Botros, M.; Chakravadhanula, V. S. K.; Kübel, C.; Bhattacharya, S. S.; Gandhi, A. S.; Hahn, H. Multicomponent Equiatomic Rare Earth Oxides. *Mater. Res. Lett.* **2017**, *5*, 102−109.

(14) Pianassola, M.; Loveday, M.; McMurray, J. W.; Koschan, M.; Melcher, C. L.; Zhuravleva, M. Solid-state synthesis of multi-component equiatomic rare-earth oxides. *J. Am. Ceram. Soc.* **2020**, *103*, 2908−2918.

(15) Cheng, B.; Lou, H.; Sarkar, A.; Zeng, Z.; Zhang, F.; Chen, X.; Tan, L.; Prakapenka, V.; Greenberg, E.; Wen, J.; Djenadic, R.; Hahn, H.; Zeng, Q. Pressure-Induced Tuning of Lattice Distortion in a High-Entropy Oxide. *Commun. Chem.* **2019**, *2*, 1−9.

(16) Tseng, K. P.; Yang, Q.; McCormack, S. J.; Kriven, W. M. High-entropy, phase-constrained, lanthanide sesquioxide. *J. Am. Ceram. Soc.* **2020**, *103*, 569−576.

(17) Ushakov, S. V.; Hayun, S.; Gong, W.; Navrotsky, A. Thermal Analysis of High Entropy Rare Earth Oxides. *Materials* **2020**, *13*, 3141.

(18) Park, T.; Javadinejad, H. R.; Kim, Y. K.; Chang, H. J.; Choi, H.; Woong, C.; Ashong, A. N.; Lee, Y. S.; Kim, J. H. Effect of Processing Route on the Crystal Structure and Physical Properties of Bixbyite High-Entropy Oxides. *J. Alloys Compd.* **2022**, *893*, 162108.
(19) Xing, Y.; Dan, W.; Fan, Y.; Li, X. Low Temperature Synthesis of High-Entropy (Y0.2Yb0.2Sm0.2Eu0.2Er0.2)2O3 Nanofibers by a Novel Electrospinning Method. *J. Mater. Sci. Technol.* **2022**, *103*, 215−220.
(20) Zhang, G.; Milisavljevic, I.; Grzeszkiewicz, K.; Stachowiak, P.; Hreniak, D.; Wu, Y. New Optical Ceramics: High-Entropy Sesquioxide X2O3 Multi-Wavelength Emission Phosphor Transparent Ceramics. *J. Eur. Ceram. Soc.* **2021**, *41*, 3621−3628.
(21) Nundy, S.; Tatar, D.; Kojčinović, J.; Ullah, H.; Ghosh, A.; Mallick, T. K.; Meinusch, R.; Smarsly, B. M.; Tahir, A. A.; Djerdj, I. Bandgap Engineering in Novel Fluorite-Type Rare Earth High-Entropy Oxides (RE-HEOs) with Computational and Experimental Validation for Photocatalytic Water Splitting Applications. *Adv. Sustainable Syst.* **2022**, *6*, 2200067.
(22) Dąbrowa, J.; Szymczak, M.; Zajusz, M.; Mikuła, A.; Moździerz, M.; Berent, K.; Wytrwal-Sarna, M.; Bernasik, A.; Stygar, M.; Świerczek, K. Stabilizing Fluorite Structure in Ceria-Based High-Entropy Oxides: Influence of Mo Addition on Crystal Structure and Transport Properties. *J. Eur. Ceram. Soc.* **2020**, *40*, 5870−5881.
(23) Yapryntsev, M. N.; Sudzhanskaya, I. V.; Lyubushkin, R. A.; Yapryntseva, E. N. Synthesis and Electric Transportation Properties of High-Entropy Oxides Based on Cerium Oxide. *IOP Conf. Ser.: Mater. Sci. Eng.* **2021**, *1014*, 012059.
(24) Sun, Y.; Xiang, H.; Dai, F. Z.; Wang, X.; Xing, Y.; Zhao, X.; Zhou, Y. Preparation and Properties of CMAS Resistant Bixbyite Structured High-Entropy Oxides RE2O3 (RE = Sm, Eu, Er, Lu, Y, and Yb): Promising Environmental Barrier Coating Materials for Al2O3f/Al2O3 Composites. *J. Adv. Ceram.* **2021**, *10*, 596−613.
(25) Sawbridge, P. T.; Waterman, N. A. On the Thermal Expansion and Crystallography of Cubic (C) and Monoclinic (B) Forms of Gd2O3 in the Temperature Range 20 to 900 °C. *J. Mater. Sci.* **1968**, *3*, 15−18.
(26) Shannon, R. D.; Prewitt, C. T. Effective Ionic Radii in Oxides and Fluorides. *Acta Crystallogr., Sect. B: Struct. Crystallogr. Cryst. Chem.* **1969**, *25*, 925−946.
(27) Toby, B. H.; Von Dreele, R. B. GSAS-II: The Genesis of a Modern Open-Source All Purpose Crystallography Software Package. *J. Appl. Crystallogr.* **2013**, *46*, 544−549.
(28) Benmore, C. J.; Weber, J. K. R. Aerodynamic Levitation, Supercooled Liquids and Glass Formation. *Adv. Phys.: X* **2017**, *2*, 717−736.
(29) Krishnan, S.; Weber, J. K. R.; Schiffman, R. A.; Nordine, P. C.; Reed, R. A. Refractive Index of Liquid Aluminum Oxide at 0.6328 μm. *J. Am. Ceram. Soc.* **1991**, *74*, 881−883.
(30) Weber, R.; Wilke, S. K.; Benmore, C. J. Containerless Techniques for In-Situ X-Ray Measurements on Materials in Extreme Conditions. *J. Phys. Soc. Jpn.* **2022**, *91*, 091008.
(31) Weber, J. K. R.; Benmore, C. J.; Jennings, G.; Wilding, M. C.; Parise, J. B. Instrumentation for Fast In-Situ X-Ray Structure Measurements on Non-Equilibrium Liquids. *Nucl. Instrum. Methods Phys. Res. Sect. A Accel. Spectrom. Detect. Assoc. Equip.* **2010**, *624*, 728−730.
(32) Weber, J. K. R.; Tamalonis, A.; Benmore, C. J.; Alderman, O. L. G.; Sendelbach, S.; Hebden, A.; Williamson, M. A. Aerodynamic Levitator for in Situ X-Ray Structure Measurements on High Temperature and Molten Nuclear Fuel Materials. *Rev. Sci. Instrum.* **2016**, *87*, 073902.
(33) Hammersley, A. P. FIT2D: a multi-purpose data reduction, analysis and visualization program. *J. Appl. Crystallogr.* **2016**, *49*, 646−652.
(34) Chikalla, T. D.; McNEILLY, C. E.; Roberts, F. P. Polymorphic Modifications of Pm2O3. *J. Am. Ceram. Soc.* **1972**, *55*, 428.
(35) Foex, M.; Traverse, J. P. Investigations about Crystalline Transformation in Rare Earths Sesquioxides at High Temperature. *Rev. Int. Hautes Temp. Refract.* **1966**, *3*, 429−453.
(36) Tresvyatkii, S. G.; Lopato, L. M.; Schwetschenko, A. W. Untersuchung Des, KAE Einflusses Hochschmelzender Oxide Der Elemente II. Gruppe Des Periodischen Systems. Auf Polymorphe Hochtem-Peratur-Umwandlungen von Oxiden Der Seltenerdelemente. *Colloq. Int. Cent. Nat. Rech. Sci.* **1971**, *205*, 247−253.
(37) Coutures, J.; Rouanet, A.; Verges, R.; Foex, M. Etude a Haute Température Des Systèmes Formes Par Le Sesquioxyde de Lanthane et Les Sesquioxydes de Lanthanides. I. Diagrammes de Phases (1400 °C < T < T Liquide). *J. Solid State Chem.* **1976**, *17*, 171−182.
(38) Mizuno, M.; Yamada, T.; Noguchi, T. Phase Diagrams of the System Al2O3-Eu2O3 and Al2O3-Gd2O3 at High Temperatures. *J. Ceram. Soc. Jpn.* **1977**, *85*, 90−95.
(39) Shevthenko, A. V.; Lopato, L. M. DTA Method Applikation to the Highest Refractory Oxide Systems Investigation. *Thermochim. Acta* **1985**, *93*, 537−540.
(40) Zinkevich, M. Thermodynamics of Rare Earth Sesquioxides. *Prog. Mater. Sci.* **2007**, *52*, 597−647.
(41) Pianassola, M.; Anderson, K. L.; Safin, J.; Agca, C.; McMurray, J. W.; Chakoumakos, B. C.; Neuefeind, J. C.; Melcher, C. L.; Zhuravleva, M. Tuning the melting point and phase stability of rare-earth oxides to facilitate their crystal growth from the melt. *J. Adv. Ceram.* **2022**, *11*, 1479−1490.
(42) Weigel, F.; Scherer, V. Die Chemie des Promethiums. *Radiochim. Acta* **1965**, *4*, 197−203.
(43) Agca, C.; Neuefeind, J. C.; McMurray, J. W.; Liu, J.; Benmore, C. J.; Weber, R. J. K.; Navrotsky, A. In Situ High-Temperature Synchrotron Diffraction Studies of (Fe,Cr,Al)3O4 Spinels. *Inorg. Chem.* **2020**, *59*, 5949−5957.
(44) Reig-I-Plessis, D.; Casavant, D.; Garlea, V. O.; Aczel, A. A.; Feygenson, M.; Neuefeind, J.; Zhou, H. D.; Nagler, S. E.; Macdougall, G. J. Structural Transition and Orbital Glass Physics in Near-Itinerant CoV_2O_4. *Phys. Rev. B* **2016**, *93*, 014437.
(45) Lepple, M.; Ushakov, S. V.; Lilova, K.; Macauley, C. A.; Fernandez, A. N.; Levi, C. G.; Navrotsky, A. Thermochemistry and phase stability of the polymorphs of yttrium tantalate, YTaO4. *J Eur Ceram Soc.* **2021**, *41*, 1629−1638.
(46) Iida, H.; Koizumi, T.; Uesu, Y.; Kohn, K.; Ikeda, N.; Mori, S.; Haumont, R.; Janolin, P. E.; Kiat, J. M.; Fukunaga, M.; Noda, Y. Ferroelectricity and Ferrimagnetism of Hexagonal YbFeO3 Thin Films. *J. Phys. Soc. Jpn.* **2012**, *81*, 024719.
(47) Cockayne, B.; Lent, B.; Abell, J. S.; Harris, I. R. Cracking in Yttrium Orthoaluminate Single Crystals. *J. Mater. Sci.* **1973**, *8*, 871−875.
(48) Lu, Y.; Wang, J.; Yang, Y.; Dai, Y.; Sun, B.; Li, S. Czochralski Growth of YAP Crystal Doped with High Tm Concentration. *J. Cryst. Growth* **2006**, *292*, 381−385.

https://doi.org/10.1021/acs.chemmater.2c03088
Chem. Mater. 2023, 35, 1116−1124